

SOLENOIDAL IMPROVEMENTS FOR THE JF12 GALACTIC MAGNETIC FIELD MODEL

JENS KLEIMANN, TIMO SCHORLEPP, LUKAS MERTEN, AND JULIA BECKER TJUS

Ruhr-Universität Bochum, Fakultät für Physik und Astronomie, Institut für Theoretische Physik IV, 44780 Bochum, Germany

Draft version June 13, 2022

ABSTRACT

The popular JF12 analytic model by Jansson & Farrar (2012) provides a quantitative description of the Galaxy’s large-scale magnetic field that is widely used in various astrophysical applications. However, both the poloidal X-type component and the spiral disk component of JF12 exhibit regions in which the magnetic divergence constraint is violated. We first propose a cure for this problem, resulting in a truly solenoidal large-scale spiral field. Second, the otherwise straight field lines of the X-type component exhibit kinks in the Galactic plane that, in addition to implying the presence of a singular current sheet, may pose difficulties for, e.g., numerical tracing of cosmic-ray particles. We propose and discuss two possible strategies to mitigate this problem. Although all corrections are kept as minimal as possible, the extended set of model parameters will have to be carefully re-adjusted in order to fully restore the agreement to observational data that the unmodified JF12 field is based on. Furthermore, the performance of our improved version of the field model is quantitatively assessed by test simulations using the CRPropa Galactic cosmic-ray propagation code.

Keywords: Galaxy: structure — magnetic fields — methods: analytical

1. INTRODUCTION

Knowing the structure of the magnetic field of the Milky Way is crucial for various applications, such as the understanding of cosmic-ray transport in the Galaxy or magnetohydrodynamic (MHD) models of Galactic evolution. Only a full description of both the turbulent and the regular components of the field enables the prediction of cosmic-ray signatures at Earth under consideration of a realistic diffusion tensor. One of the more recent approaches to a full description on the basis of analytic equations was developed by Jansson & Farrar (2012, hereafter JF12). An improved version of the JF12 model was developed and applied – although not described in full detail – more recently by Unger & Farrar (2017, 2019). As of today, the JF12 field and its updates represent the most complete analytic description of the global Galactic magnetic field.

The “regular,” large-scale part of the JF12 model comprises four field components: a spiral disk field, a molecular ring inside the spiral field, a toroidal halo field, and a poloidal X-shaped field. An additional “striated” component is parameterized as scaling uniformly with the regular field. Jansson & Farrar (2012), who were the first to include an X-shaped component into their model, also rightfully stressed the importance of obeying Maxwell’s magnetic solenoidality constraint

$$\nabla \cdot \mathbf{B} = 0 \quad (1)$$

but, upon closer inspection, do not meet the latter requirement at all boundaries. An alternative family of Galactic magnetic field (GMF) models fully satisfying Equation (1) was developed by Ferrière & Terral (2014) and later adjusted to constraints from observational data by Terral & Ferrière (2017). More recently, Shukurov et al. (2019) presented a parameterized GMF model based on magnetic diffusion and mean-field dynamo theory. Unlike the upcoming IMAGINE project

(Boulanger et al. 2018), which aims at the development of a completely revised GMF model by combining current observational data from various sources with modern Bayesian analysis, this work does not present a completely new model. Instead, we suggest a gradual improvement of the existing JF12 model, although the employed ideas might well be used in future GMF models.

The paper is organized as follows. After this present introduction, Section 2 describes and discusses two methods to turn JF12’s spiral field component into a truly solenoidal version of itself. A much simpler solution is then offered for a similar problem with the X-type field component in Section 3, which then presents two possible modifications to remove the sharp kinks of field lines at the Galactic plane while still maintaining solenoidality. Section 4 contains a performance comparison of the old vs. the new field model using simulations of propagating particles, and Section 5 concludes the paper with a summary. Throughout this paper, only the spiral disk and the X-field will be addressed. Neither the molecular ring, nor the toroidal halo field or the two turbulent components are subject to investigation in this paper.

2. A TRULY SOLENOIDAL SPIRAL DISK

2.1. Motivation

We argue that it is vital for a GMF model to be completely void of magnetic monopoles both globally and locally at least for the following two reasons. First, depending on the application at hand and the methods employed therein, even small non-zero values of $|\nabla \cdot \mathbf{B}|$ may give rise to unphysical effects such as negative pressures or densities, violation of momentum or energy conservation, or the rise of spurious waves (e.g. Brackbill & Barnes 1980), specifically in the context of MHD simulations, including cases where the magnetic field is not actually evolved but treated as a static background.

Second, due to our fixed position within the Galaxy and the fact that only line-of-sight observations from this solitary vantage point are available, our Galaxy’s global properties

jk@tp4.rub.de
timo.schorlepp@rub.de
lukas.merten@rub.de
julia@tp4.rub.de

(such as shape, geometry, and magnetic field structure, to name but a few) are inherently difficult to constrain. Intrinsic ambiguities have to be resolved through inversion and parameter fitting. It is therefore all the more important to use as many physical constraints as possible. In that vein, the unconditional validity of Maxwell's equations, and in particular of Equation (1), is clearly undisputed and provides rather tight constraints on the set of physically admissible field models, as was already noted by Jansson & Farrar (2012). The effect is expected to be strongest for studies sensitive to spurious magnetic monopoles. Even in other cases, the use of a completely solenoidal field model is to be preferred for its higher degree of physical realism. In particular, it is important to keep in mind that violations of Equation (1), even those that are limited to a spatial volume of measure zero, will often have far-reaching consequences also for more distant regions. This latter point will be illustrated in this paper on the basis of the marked differences between GMF models which conserve magnetic flux and those that do not.

2.2. Properties of the JF12 Spiral Disk Field

We begin by briefly summarizing the basic properties of the original JF12 spiral disk component, taking the opportunity to properly write up the relevant equations. In the disk region between $r_1 = 5$ and $r_2 = 20$ kpc, a field line passing through a point with supergalactic cylindrical coordinates (r_a, φ_a, z_a) follows a logarithmic spiral

$$r(\varphi) = r_a \exp[(\varphi - \varphi_a) \tan i] \quad (2)$$

with a uniform inclination angle $i = 11.5^\circ$, as depicted in the left panel of Figure 3. The spiral is partitioned into eight field line-delimited regions of relative widths f_j summing to $\sum_{j=1}^8 f_j = 1$ (actually to 0.999 due to round-off errors), with corresponding field strengths b_j at the inner rim r_1 . The field strength parameters $b_{1...7}$ are fitted to data, while b_8 is chosen such that

$$\sum_{j=1}^8 b_j f_j = 0 \quad (3)$$

holds, implying that the total magnetic flux passing through a co-axial cylindrical shell of any radius is zero. The field strength in spiral region j is equal to $(r_1/r) b_j$. While this, together with constraint (3), is sufficient to warrant magnetic solenoidality within the disk, field lines will still “start” and “end” at the inner and outer spiral disk boundaries, i.e., Maxwell's divergence constraint (1) is violated along these boundaries, despite occasional claims to the contrary (e.g. Jansson & Farrar 2012; Beck et al. 2016; Unger & Farrar 2019). We understand the spiral field's confinement to the annulus $r \in [r_1, r_2]$ to be motivated by the fact that the underlying data analysis would not allow the field to be adequately constrained beyond these radii, implying the need to substitute a suitable solenoidal continuation before employing the field in a particular scientific investigation. In this vein, we propose and discuss possible solutions to this crucial issue in Section 2.4.

2.3. Explicit Component Formulas

Since JF12 provide explicit formulas only to some extent and partially content themselves with mere recipes for the

construction of the actual field components, we use the opportunity to provide these formulas here for completeness and later reference, and in a form that will be more suitable for the purpose at hand.

JF12 specify the border between adjacent spiral regions by means of the radius r_{-x} at which a spiral boundary intersects the negative x -axis. We note in passing that their spiral equation $r = r_{-x} \exp[\varphi \tan(90^\circ - i)]$ should actually read $r = r_{-x} \exp[(\varphi - \pi) \tan i]$ since it would otherwise relate r_{-x} to the $(\varphi = 0)$ direction, i.e., the *positive* x -axis, and would furthermore result in a much larger inclination angle of $90^\circ - i = 78.5^\circ$ that would have field lines pointing outwards almost radially.

This functional form and the value for i were adopted from the earlier model by Brown et al. (2007), although these authors do not cite explicit values for r_{-x} . For our purpose, and possibly for other applications as well, it is instead more convenient to work in terms of the azimuthal angle $\varphi = \Phi_{1,j}$ at which the limiting field line $r_j(\varphi)$ between two adjacent regions j and $j - 1$ intersects the inner spiral disk boundary at $r_1 = 5$ kpc. (For the remainder of this paper, all lengths are in units of kpc unless indicated otherwise.) These two descriptions are related through

$$\frac{r_{-x,j}}{r_1} = \frac{r_j(\pi)}{r_j(\Phi_{1,j})} = \exp[(\pi - \Phi_{1,j}) \tan i], \quad (4)$$

and the relative width of spiral region j is

$$f_j = (\Phi_{1,j-1} - \Phi_{1,j}) / (2\pi) \quad (5)$$

with $\Phi_{1,0} \equiv 2\pi + \Phi_{1,8}$ for cyclic closure. Table 1 summarizes the obtained values. Note that we take azimuthal coordinates in $[-\pi, \pi]$ instead of the more conventional $[0, 2\pi]$. This is done to keep the sequence of $\Phi_{0,j}$ in strictly descending order.

The explicit magnetic field components at an arbitrary position (r, φ) within the spiral disk can be obtained by first mapping the point along its field line back to the inner rim at

$$(r_1, \varphi_1) = \left(r_1, \varphi - \frac{\ln(r/r_1)}{\tan i} \right), \quad (6)$$

looking up the spiral region $j = j(\varphi_1)$ that φ_1 is situated in, and setting the field to

$$\begin{aligned} [B_r, B_\varphi] &= \frac{b_j r_1}{r} [\sin i, \cos i] \\ &= B_{r_1} \left(\varphi - \frac{\ln(r/r_1)}{\tan i} \right) \frac{r_1}{r} [\sin i, \cos i] \end{aligned} \quad (7)$$

where $B_{r_1}(\varphi)$ is the periodic step function that maps $\varphi \in [\Phi_{1,j-1}, \Phi_{1,j}]$ to b_j , see Figure 1. For heights $z > 0$ ($z < 0$) above (below) the Galactic plane, an additional factor

$$\Lambda(z) \equiv 1 - L(z, h, w) \equiv \left[1 + \exp\left(\frac{|z| - h}{w/2}\right) \right]^{-1} \quad (8)$$

with parameters $[h, w] = [0.4, 0.27]$ kpc is added to the right hand side of Equation (7). Since this factor does not depend on (r, φ) and is therefore immaterial to the question of magnetic flux conservation, it will be neglected in the following, thus restricting our ensuing considerations of the spiral disk to the Galactic ($z = 0$) plane.

The above formulation has the clear advantage that the solenoidal correction that will be described in the next section can easily be applied to an existing implementation of the

j	1	2	3	4	5	6	7	8
b_j [μG]	0.1	3.0	-0.9	-0.8	-2.0	-4.2	0.0	2.7
$r_{-x,j}$	5.1	6.3	7.1	8.3	9.8	11.4	12.7	15.5
f_j	0.130	0.165	0.094	0.122	0.130	0.118	0.084	0.156
$\Phi_{1,j}/\pi$	0.969	0.638	0.451	0.207	-0.053	-0.289	-0.458	-0.770

Table 1

Width parameters for the eight spiral regions. Rows 1 to 3 reproduced from JF12, row 4 from this work.

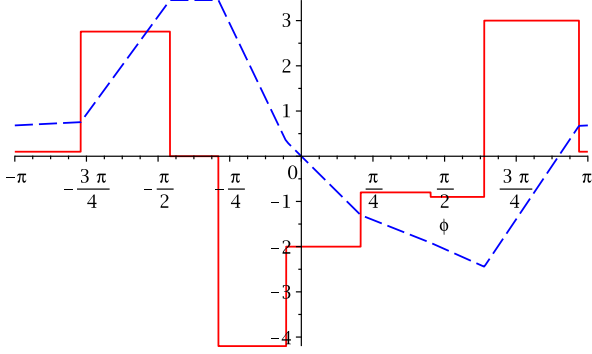


Figure 1. Step function $B_{r_1}(\varphi)$ (red, solid) and its integral $H(\varphi)$ (blue, dashed) as used in Equation (12) evaluated at $r = r_1$, with lower interval bound $\varphi_0 = 0$. A different bound φ'_0 would shift the blue curve vertically until $B_{r_1}(\varphi'_0) = 0$ is satisfied.

JF12 field that should have $B_{r_1}(\varphi) = \|\mathbf{B}\|_{r=r_1}$ readily accessible.

2.4. Clearing Divergences at the Spiral Boundaries

The general idea behind our proposed method to make the spiral field fully divergence-free is to first define a new parameter $\delta > 0$ and to use the unmodified spiral field only within the central part of the disk at $r \in [r_1 + \delta, r_2 - \delta]$, while the radial intervals $[r_1, r_1 + \delta]$ and $[r_2 - \delta, r_2]$ form circular annular regions of width δ at both boundaries, in which incoming and outgoing flux is smoothly redistributed. For simplicity of the argument, we take the values of δ at the inner and outer boundary to be the same, but still note that they could easily be chosen differently for a given application. For the outer rim r_2 , an alternative treatment not involving a transition region will be described towards the end of this section.

Spiral field lines traversing radii $r_1 + \delta$ and $r_2 - \delta$ do so at inclination i , and are to be smoothly continued into the respective transition regions. In a first step, the factor r_1/r in Equation (7) is replaced by a polynomial $p_\delta(r)$ inside the transition regions, leading to

$$[\bar{B}_r, \bar{B}_\varphi] = B_{r_1} \left(\varphi - \frac{\ln(r/r_1)}{\tan i} \right) p_\delta(r) [\sin i, \cos i]. \quad (9)$$

From here onwards, a symbol with a bar denotes quantities introduced in addition to JF12, while those without a bar are the original ones from that paper. Here, $p_\delta(r)$ is a second-order polynomial whose coefficients are fixed by requiring \bar{B}_r to be differentiable at the limiting radius $r_\beta = r_1 + \delta$ ($r_\beta = r_2 - \delta$) separating the intermediate, unmodified region from the inner (outer) transition region, and to vanish at $r = r_1$ ($r = r_2$), where the entire spiral disk ends. These requirements result in the explicit expression

$$p_\delta(r) = \frac{r_1}{r_\beta} \left[2 - \frac{r}{r_\beta} + \left(\frac{r_\alpha}{r_\beta} - 2 \right) \left(\frac{r - r_\beta}{r_\alpha - r_\beta} \right)^2 \right] \quad (10)$$

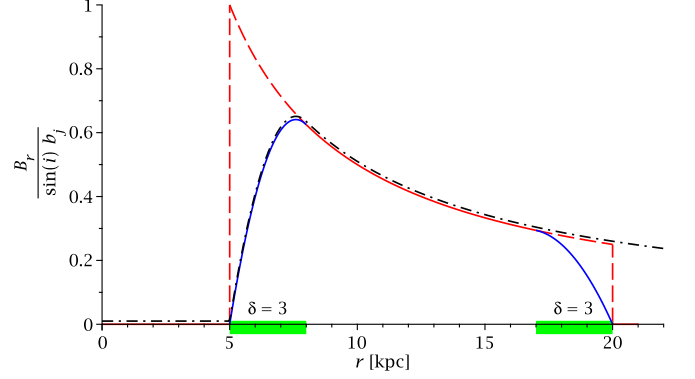


Figure 2. JF12's normalized B_r profile r_1/r (red dashed and dotted) and polynomial inserts $p_\delta(r)$ (blue) within the two transition regions (indicated by green bars) of width $\delta = 3$ kpc. The new total compound profile (employing azimuthal flux redistribution at both the inner and outer edge) is composed of the respective contributions drawn in solid linestyle (red and blue). As an alternative, the spiral disk could be extended to infinity via $r_2 \rightarrow \infty$ (black, dash-dotted).

at the inner ($r_\alpha = r_1$, $r_\beta = r_1 + \delta$) and outer ($r_\alpha = r_2$, $r_\beta = r_2 - \delta$) rim of the spiral disk. Figure 2 serves to illustrate the situation.

Up until now, we have merely modified the peripheral regions of the spiral disk in a way that lets its field strength smoothly tend to zero while avoiding kinking field lines. In order to determine the additional φ component $B_{\varphi, \text{add}}$ that ensures magnetic solenoidality within the transition regions, we use

$$0 = \nabla \cdot \bar{\mathbf{B}} = \frac{1}{r} \left(\frac{\partial(r \bar{B}_r)}{\partial r} + \frac{\partial(\bar{B}_\varphi + \bar{B}_{\varphi, \text{add}})}{\partial \varphi} \right) \quad (11)$$

and Equation (9) to get

$$\bar{B}_{\varphi, \text{add}} = - \underbrace{\frac{\partial[r p_\delta(r)]}{\partial r}}_{\equiv q_\delta(r)} H \left(\varphi - \frac{\ln(r/r_1)}{\tan i} \right) \sin i \quad (12)$$

with

$$H(\varphi) = \int_{\varphi_0}^{\varphi} B_{r_1}(\varphi') d\varphi'. \quad (13)$$

The first factor of Equation (12) can be evaluated straightforwardly from Equation (10) as

$$q_\delta(r) = \frac{r_1}{r_\beta} \left[2 - 2 \frac{r}{r_\beta} + \left(\frac{r_\alpha}{r_\beta} - 2 \right) \frac{3r^2 - 4r_\beta r + r_\beta^2}{(r_\alpha - r_\beta)^2} \right] \quad (14)$$

and the integral $H(\varphi)$ yields a piecewise linear, 2π -periodic function of φ . The lower interval bound φ_0 may be interpreted as the azimuthal direction at which an impenetrable wall with inclination i , separating magnetic flux being redirected into clockwise and counter-clockwise directions, intersects $r = r_1$. Its value may be chosen freely, one possibility

being a choice that minimizes the maximum or average value of additional azimuthal magnetic flux or energy that is brought into the system. For simplicity, Figure 1 uses the ad hoc value $\varphi_0 = 0$ that apparently results in a rather balanced distribution. In total, the transition zone field is to be set as

$$\bar{\mathbf{B}}_{\text{tr}} = \bar{B}_r \mathbf{e}_r + [\bar{B}_\varphi + \bar{B}_{\varphi, \text{add}}] \mathbf{e}_\varphi \quad (15)$$

with components given by Equations (9) and (12).

Identifying the most appropriate choice for the transition thickness δ is not straightforward. A small value will leave most of the disk field unchanged, which could be a desirable strategy in order to minimize interference with the delicate agreement with observational data. On the other hand, the combined azimuthal flux of field lines being tightly packed into two very thin transition zones may then become unreasonably large. For the intermediate value of $\delta = 3.0$ kpc, the added azimuthal flux from $\bar{B}_{\varphi, \text{add}}$ is comparable to the reduction in spiral flux which arises due to the magnitude of $p_\delta(r)$ being considerably smaller than r_1/r in the region of interest, as can clearly be seen in Figure 2.

Since the presented method of flux redistribution inside the disk is of course not the only way to ensure a divergence-free field, one may ask at this point how it compares to other strategies. For instance, one could also divert field lines away from the Galactic plane and into the halo, similarly to how Ferrière & Terral (2014) avoid infinite field strengths at their model’s polar axis. Our reasons to consider the disk in isolation is that it allows us to stay conceptually closer to the JF12 model, and in particular to take advantage of the total balance of incoming and outgoing flux expressed in Equation (3).

While some form of flux rearrangement is inevitable at the inner rim, yet a different option could be exploited at the outer rim by simply moving its position from $r_2 = 20$ kpc to infinity (or, from a more practical point of view, beyond the specific boundaries of the region under consideration), such that the field strength continues to decay as $1/r$ indefinitely. Since with this radial profile, the field strength at, say, $r = 25$ kpc would still amount to 20% of its reference value at r_1 , it is clear that either option would represent a marked deviation from the original JF12 disk field. A reassessment via fitting to observables, ideally including both δ and r_2 as yet two more free parameters, will therefore in any case be mandatory, and in this sense, the two possibilities outlined above represent the limiting cases in (δ, r_2) parameter space. This task, however, is beyond the scope of this present work, which merely seeks to present and discuss a subset of physically admissible options.

While we do acknowledge that an indefinite $1/r$ decay is a simple and widely accepted possibility in the community, one should be very aware of the conceptual and practical implications of a galactic disk whose magnetic field is truly unbounded in spatial extent. Specifically, the total energy

$$W_{B, \text{disk}} \propto \int_{-\infty}^{\infty} \int_{r_1}^{r_2} \left(\frac{\Lambda(z)}{r} \right)^2 r dr dz = C \ln \left(\frac{r_2}{r_1} \right) \quad (16)$$

contained in the magnetic field of such a disk (with $C \approx 0.557$ arising from vertical integration) obviously diverges as $r_2 \rightarrow \infty$, leading to what could be called a “magnetic Olbers’ paradox.” Even if this limit may not actually be realized in most practical applications, it still seems conceivable that the excess of energy thus implied may have a distorting effect on, for instance, cosmological simulations involving large volumes populated with galactic disks, or line-of-sight integra-

tions connecting the observer to distant galaxies.

Figure 3 compares the old and new spiral field structure for both strategies, and also uses a second row of plots to illustrate the general idea of flux being redistributed. These plots seem to suggest that the unmodified JF12 spiral field is recovered in the limit $\delta \rightarrow 0$. While this is indeed the case within the open annulus $r_1 < r < r_2$, the additional azimuthal flux would then accumulate to form a singular, infinitely strong flux ring in the transition region of zero width, which would be just as unphysical (although for a different reason) as cutting all field lines at the radial boundaries.

We note that, as can be seen by carefully inspecting the lower middle plot of Figure 3, field lines may kink when crossing the boundary between spiral regions. This is unavoidable near $r = r_\beta$ due to the discontinuous transitions between these regions that are an inherent feature of the JF12 model. Further into the transition regions, this could in principal be avoided by replacing the piecewise constant integrand in Equation (12) by a smoothed version of itself in a way that increases the smoothing length from zero at r_β to a finite value towards r_α . However, presenting and discussing appropriate formulas to this end is beyond the scope of this paper as well.

3. IMPROVEMENTS FOR THE X-TYPE FIELD COMPONENT

In this section, we turn our attention away from the disk and towards the poloidal component, first noting another divergence-related problem with the latter, which is fortunately much easier to solve. The remainder of the section deals with the problem of kinking field lines and discusses two appropriate mitigation strategies.

3.1. Explicit Formulas

As with the spiral field, we also briefly list explicit formulas for the components $[B_r, B_z]$ of the poloidal X-field, both for later reference and because not all of them have been provided explicitly in the literature. The X-field is characterized by straight field lines whose elevation angle $\Theta_X \equiv \arctan(B_z/B_r)$ varies as follows. A field line intersecting the midplane $z = 0$ at radius r_p has

$$\tan \Theta_X = \tan \Theta_X^0 \times \begin{cases} r_X^c/r_p & : r_p < r_X^c \\ 1 & : r_p \geq r_X^c \end{cases} \quad (17)$$

with global constants r_X^c and Θ_X^0 , and B_r changes sign at the midplane, such that $B_r/z > 0$. Note that, according to this equation, it is $\cot \Theta_X$, rather than the inclination Θ_X itself, that depends linearly on r_p in the “linear” region.

The easiest way to obtain cylindrical components $[B_r, B_z]$ at given (r, z) is to first compute $\tilde{r}_p \equiv r - |z| \cot \Theta_X^0$ and then define

$$r_p \equiv \begin{cases} \tilde{r}_p & : r > \tilde{r}_p \\ r r_X^c / (r_X^c + |z| \cot \Theta_X^0) & : r \leq \tilde{r}_p \end{cases} \quad (18)$$

and further

$$[B_r, B_z] \equiv \frac{b_X(r_p)}{(r/r_p)^d} [\text{sgn}(z) \cos \Theta_X, \sin \Theta_X] \quad (19)$$

with an absolute field strength

$$b_X(r_p) = B_X \exp(-r_p/r_X) \quad (20)$$

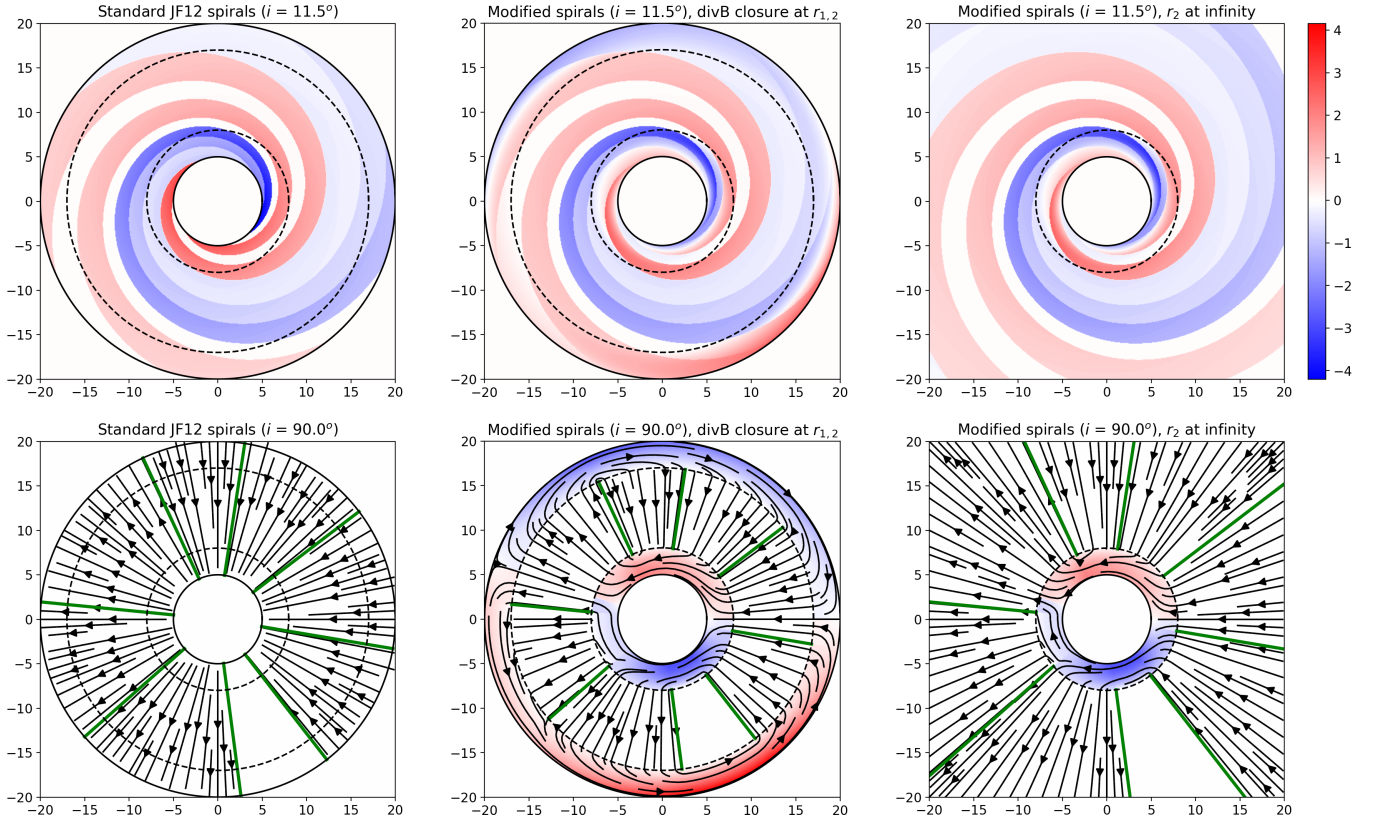


Figure 3. Contour plots of magnetic field strength multiplied with the sign of B_ϕ , such that negative (positive) values indicate clockwise (counter-clockwise) field orientation. The top row uses the actual inclination angle of $i = 11.5^\circ$, while the bottom row shows segments of field lines for the hypothetical case of 90° inclination, illustrating the concept of flux redistribution in the inner and outer transition regions, whose width is uniformly chosen as $\delta = 3$ kpc. Green radial lines visually separate the eight “spiral” regions, across which the field orientation may change from inward- to outward-directed. Left: the original JF12 configuration, essentially reproducing the upper left plot of Figure 7 from that paper. Middle: the modified, and thus fully solenoidal, field for a transition width of $\delta = 3$ kpc (bounded by dashed lines). Right: An alternative treatment for the outer rim, whose position r_2 moves from 20 kpc to infinity, allowing field lines (of vanishing field strength) to “close” there. Note the straight field line at $\varphi = \varphi_0 = 0 \Leftrightarrow y = 0, x > 0$ separating left- and right-going flux. The fact that field lines seem to have endpoints is an artefact of the employed plotting procedure. Note also that the color bar is not relevant for the bottom row of plots, whose maximum absolute field strength is larger than that of the other two cases by a factor of about three.

at $z = 0$, and an exponent

$$d \equiv \begin{cases} 2 & : r_p < r_X^c \\ 1 & : r_p \geq r_X^c \end{cases} \quad (21)$$

that reflects the different scaling which the solenoidality condition (1) enforces in the two regions.

3.2. Solenoidality Near the Origin and at Large Distances

The X-type field of JF12 omits a spherical region of radius 1 kpc around the origin, in which the field is set to zero. We note, however, that despite the seemingly divergent scaling of Equation (19) as $r \rightarrow 0$, the field components remain perfectly well-defined also on the z -axis, where they smoothly converge to

$$\lim_{r \rightarrow 0} [B_r, B_z] = \left[0, B_X \left(1 + \frac{|z|}{r_X^c \tan \Theta_X^0} \right)^{-2} \right] \quad (22)$$

with the field strength attaining its global, finite maximum value of B_X right at the origin. This can be seen by noting that, according to Equation (9) in JF12, r_p/r is actually independent of r in the “linear” region and may by straightforwardly evaluated at any z , including $z = 0$. For this reason,

we assume in the following that the field (19) is being continued also inside the previously excluded central region within 1 kpc of the origin. This is justified not only by simplicity (and, above all, as the canonical means to restore the otherwise violated solenoidality at the surface of the “exclusion sphere”), but also by the fact that, as stated in JF12, the employed RM data does not permit to constrain the central part of the field in a useful way.

Finally, we note that, since the JF12 X-field, just like its spiral disk field, is set to zero outside a cylinder of 20 kpc radius around the $r = 0$ axis, the question again arises as to how solenoidality should best be restored at this outer cylindrical rim surface. One straightforward possibility is to depart from the original prescription by *not* cutting the field at a finite cylindrical radius and instead letting its field strength decay as $1/r$ (or $1/r^2$, depending on direction) instead. The second alternative would again consist in a redistribution of field lines that would then likely assume a dipole-like structure as flux needs to be transported from the Northern to the Southern Galactic half-space. Since there are currently no observational indications for a departure from the X-shape structure at large distances from the Galactic center, we refrain from making explicit suggestions for such a formal closure at this point. We merely note that, as with the spiral field, some form of field line closure is clearly

desirable – if not mandatory – for fundamental reasons, and that the discrimination between different methods and their respective parameters should again be inferred based on observational constraints.

3.3. Motivating the Need for a Kink-free X-field

The inclusion of the X-type field into JF12 was motivated by corresponding radio observations of edge-on galaxies (e.g. Beck 2009), and the simplest way to model this feature is to employ field lines which are straight on either side of the Galactic plane, where they meet to form wedge-shaped kinks. While this may be a very reasonable approximation for many applications, it does harbor problems for others. For instance, the associated current sheet of infinite strength at the $z = 0$ plane is unphysical, and will thus tend to generate equally unphysical forces in MHD simulations. To see this, we may approximate the kink as the limiting case of a smooth, X-shaped, and dimensionless poloidal field

$$\mathbf{B}^* = \arctan(z/\eta) \mathbf{e}_r + \mathbf{e}_z, \quad (23)$$

which has a finite radius of curvature η at $z = 0$, as well as an – for this purpose irrelevant – asymptotic inclination angle of $\arctan(2/\pi) \approx 32^\circ$. At $z = 0$, the respective dimensionless expressions for the associated densities of electric current and Lorentz force are then found from

$$\mathbf{J}^*|_{z=0} = (\nabla \times \mathbf{B}^*)|_{z=0} = \frac{\eta}{\eta^2 + z^2} \Big|_{z=0} \mathbf{e}_\varphi = \frac{1}{\eta} \mathbf{e}_\varphi \quad (24)$$

$$\mathbf{F}_L|_{z=0} = (\mathbf{J}^* \times \mathbf{B}^*)|_{z=0} = \frac{1}{\eta} \mathbf{e}_r, \quad (25)$$

both of which diverge as $\eta \rightarrow 0$. Note that this line of reasoning is not affected by the non-zero value of $\nabla \cdot \mathbf{B}^*$.

Another instance in which smooth field lines are preferred over kinking ones is the numerical tracing of charged particles, where the necessarily finite step size makes it difficult to accommodate rapid or even discontinuous changes in field strengths along the trajectory of a particle that would otherwise simply follow its original field line.

With this motivation in mind, we now proceed to present two modifications that keep the radius of curvature finite within a planar region around the midplane, while the field outside this region is largely left unchanged, with field lines smoothly traversing the boundaries between those regions. This ensures that the desired result is obtained while again keeping the unavoidable interference with JF12's fine-tuned set of parameters at a minimum.

3.4. Method I: Parabolic Replacement Near the Disk

3.4.1. General Idea and Formulas

We first consider the more general case of a largely arbitrary source field \mathbf{B} , which we merely require to obey symmetry relations $B_r(r, -z) = -B_r(r, z)$ and $B_z(r, -z) = B_z(r, z)$, and only later specialize to the JF12 X-field. The goal is to leave \mathbf{B} unchanged outside a freely chosen reference height $|z| \geq z_s > 0$ (thereby ensuring that the original \mathbf{B} is fully recovered in the limit $z_s \rightarrow 0$), but create a replacement field $\bar{\mathbf{B}}$ inside $|z| < z_s$ whose field lines are given by parabolas

$$r_F(r_s, z) \equiv a(r_s) + b(r_s)z^2 \quad (26)$$

which are parameterized by the radius r_s at which the respective field line passes $|z| = z_s$, smoothly connecting to its outer counterpart. This parameterization is analogous to the one using r_p (except for the finite, rather than zero, reference height), and both are in fact related via

$$(r_s - r_p) \tan \Theta_X = z_s. \quad (27)$$

The coefficient functions $a(r_s)$ and $b(r_s)$ are fixed by requiring that field lines be continuous and differentiable at height z_s via

$$r_F(r_s, z_s) = r_s \quad (28)$$

$$\frac{\partial r_F(r_s, z)}{\partial z} \Big|_{z_s} = \frac{B_r}{B_z} \Big|_{(r_s, z_s)} \quad (29)$$

yielding

$$r_F(r_s, z) = r_s - \frac{1}{2} \left(z_s - \frac{z^2}{z_s} \right) \frac{B_r(r_s, z_s)}{B_z(r_s, z_s)}. \quad (30)$$

We then use once more the definition of field lines (this time for $|z| < z_s$) to obtain

$$\frac{\bar{B}_r(r_F(r_s, z), z)}{\bar{B}_z(r_F(r_s, z), z)} = \frac{\partial r_F(r_s, z)}{\partial z} = \left(\frac{z}{z_s} \right) \frac{B_r(r_s, z_s)}{B_z(r_s, z_s)} \quad (31)$$

by differentiating our newly found Equation (30). We see that indeed, $\bar{B}_r \rightarrow 0$ as $|z| \rightarrow 0$, and also that \bar{B}_r 's change of sign at the midplane is maintained.

Next, we exploit the divergence constraint by considering the conservation of magnetic flux

$$2\pi r \, dr \, \bar{B}_z(r, z) = 2\pi r_s \, dr_s \, B_z(r_s, z_s) \quad (32)$$

from an arbitrary height $z < z_s$ to $z = z_s$ through a circular, disk-parallel annulus of infinitesimal radial width dr along a field line passing through a given position (r, z) . Here, r_s is the parameter of the parabola passing through (r, z) , and is therefore to be obtained from the condition $r = r_F(z)$ using Equation (30). At height z , the radial width of the annulus bounded by adjacent parabolic field lines r_s and $r_s + dr_s$ is

$$dr = r_F(r_s + dr_s, z) - r_F(r_s, z) = \frac{\partial r_F(r_s, z)}{\partial r_s} dr_s \quad (33)$$

when neglecting terms of order $\mathcal{O}(dr_s^2)$. Therefore, Equation (32) implies

$$\begin{aligned} F(r, z, r_s) &\equiv \frac{\bar{B}_z(r, z)}{B_z(r_s, z_s)} = \frac{r_s/r}{\left(\frac{\partial r_F(r_s, z)}{\partial r_s} \right)} \\ &= \frac{1 + \frac{1}{2r} \left(z_s - \frac{z^2}{z_s} \right) \frac{B_r(r_s, z_s)}{B_z(r_s, z_s)}}{1 - \frac{1}{2} \left(z_s - \frac{z^2}{z_s} \right) \frac{\partial}{\partial r_s} \left[\frac{B_r(r_s, z_s)}{B_z(r_s, z_s)} \right]} \end{aligned} \quad (34)$$

and, together with Equation (31),

$$\begin{aligned} \bar{\mathbf{B}}(r, z) &= \left[\left(\frac{z}{z_s} \right) B_r(r_s, z_s) \mathbf{e}_r + B_z(r_s, z_s) \mathbf{e}_z \right] \\ &\quad \times F(r, z, r_s). \end{aligned} \quad (35)$$

Further evaluation of this equation is precluded by the fact that the implicit Equation (30) cannot be solved for r_s in this

general form.

3.4.2. Application to JF12

Using Equation (17) for the case of JF12, the field line equation (30) becomes

$$r_F(r_s, z) = r_s - \frac{z_s}{2 \tan \Theta_X^0} \left(1 - \frac{z^2}{z_s^2} \right) \times \begin{cases} r_s/r_s^c & : r_s < r_s^c \\ 1 & : r_s \geq r_s^c \end{cases} \quad (36)$$

when expressed in terms of r_s . Here,

$$r_s^c \equiv r_X^c + z_s / \tan \Theta_X^0 \quad (37)$$

is the radius at which the ‘‘critical’’ straight field line, defined as the one separating both regions and crossing $z = 0$ at radius r_X^c , intersects the $z = z_s$ plane. We can see from Equation (36) that in the outer region ($r \geq r_s^c$), the parabolas are identical except for a translation in r , while in the inner region, they are additionally compressed in the r direction, becoming straight and vertical at the $r = 0 = r_s$ axis.

To construct the new field \mathbf{B} at position (r, z) within $|z| \leq z_s$, we first need to find the parameter r_s of the corresponding parabola. Assuming $r_s \geq r_s^c$ in Equation (36), the condition $r = r_F(r_s, z)$ may be trivially solved for r_s , giving

$$r_s = r + \frac{r_X^c}{\beta_0} \left(1 - \frac{z^2}{z_s^2} \right) \quad (38)$$

with $\beta_0 \equiv 2(r_X^c \tan \Theta_X^0)/z_s$ a constant. If the assumption $r_s \geq r_s^c$ turns out to be correct for the point in question, Equation (38) gives the desired r_s , else Equation (36) points us to

$$r_s = r \left[1 - \frac{1}{2 + \beta_0} \left(1 - \frac{z^2}{z_s^2} \right) \right]^{-1} \quad (39)$$

for the ‘‘inside’’ case. Using relation (27) between r_p and r_s , we have for the inner region

$$\frac{1}{\tan \Theta_X} = \frac{1}{\tan \Theta_X^0} \frac{r_p}{r_X^c} = \frac{1}{r_X^c \tan \Theta_X^0} \left(r_s - \frac{z_s}{\tan \Theta_X} \right), \quad (40)$$

which may be solved to yield

$$\frac{1}{\tan \Theta_X} = \frac{r_s}{r_X^c \tan \Theta_X^0 + z_s}, \quad (41)$$

and further

$$\frac{\partial}{\partial r_s} \left[\frac{B_r(r_s, z_s)}{B_z(r_s, z_s)} \right] = \frac{\partial}{\partial r_s} \left[\frac{1}{\tan \Theta_X|_{(r_s, z_s)}} \right] = \frac{1}{r_X^c \tan \Theta_X^0 + z_s}. \quad (42)$$

In the outer region, where $\Theta_X = \Theta_X^0$ is a constant, this derivative vanishes. Finally, we are ready to fully evaluate Equation (35) and determine F as

$$F(r, z) = \begin{cases} \left[1 - \frac{1}{2 + \beta_0} \left(1 - \frac{z^2}{z_s^2} \right) \right]^{-2} & : \text{inside} \\ 1 + \frac{1}{\beta_0} \left(\frac{r_X^c}{r} \right) \left(1 - \frac{z^2}{z_s^2} \right) & : \text{outside} \end{cases} \quad (43)$$

in the two regions. The third argument r_s in F has now been suppressed because $r_s = r_s(r, z)$ was inserted from Equation (36).

In summary, the procedure to evaluate the improved field at arbitrary (r, z) for a global choice of z_s is as follows:

1. Discriminate between ‘‘inner’’ and ‘‘outer’’ region as before, but replacing the criterion $r_p < r_X^c$ by $r_s < r_s^c$ within $|z| < z_s$.
2. If $|z| < z_s$, compute r_s using either Equation (38) or (39), depending on whether $r_s \geq r_s^c$ or not.
3. Compute the standard field at (r_s, z_s) , then the new field $\tilde{\mathbf{B}}$ at (r, z) using Equations (35) and (43).

Figure 4 serves to illustrate the result thus obtained.

3.5. Method II: Smoothing via Convolution

A ‘‘global’’ alternative to the smoothing approach which was previously discussed is a convolution of the JF12 X-field with a smooth kernel function $K \in C_0^\infty(\mathbb{R}^3)$, a so-called ‘‘mollifier.’’ The convolution of the Cartesian field components B_c , $c \in \{x, y, z\}$ is given as

$$\begin{aligned} \tilde{B}_c(\mathbf{r}) &= (B_c * K)(\mathbf{r}) \\ &= \int_{\text{supp}(K)} B_c(\mathbf{r} - \mathbf{r}') K(\mathbf{r}') d^3 r'. \end{aligned} \quad (44)$$

This integral operation will always yield a smooth C^∞ field if the initial field is locally integrable, so this method is not restricted to the field configuration at hand. Furthermore, it preserves the solenoidality of the initial field, which may be checked using the identity

$$\frac{\partial}{\partial x_k} (B_c * K)(\mathbf{r}) = \left(\frac{\partial B_c}{\partial x_k} * K \right)(\mathbf{r}) \quad (45)$$

that holds for any differentiable function B_c within the compact support of K . We use the standard mollifier

$$K(\mathbf{r}) = \begin{cases} \mathcal{N} \exp \left[\frac{1}{(\|\mathbf{r}\|/w_X)^2 - 1} \right] & : \|\mathbf{r}\| < w_X \\ 0 & : \|\mathbf{r}\| \geq w_X \end{cases} \quad (46)$$

where w_X denotes the radius of the kernel’s compact support, and \mathcal{N} normalizes the function. The convolution averages the initial field inside a sphere of radius w_X with K as a weight function. As it is not possible to calculate the integral in Equation (44) analytically for the functions at hand, the convolution was computed numerically on the grid points of a (r, z) grid with a spatial resolution of 10 pc and $0 \leq r, z \leq 20$ kpc for this paper. SciPy’s (Oliphant 2007) `tplquad` function in Python 2.7 was used to directly evaluate the volume integrals at these points in the $y = 0$ plane, where $\tilde{B}_r = \tilde{B}_x$ and $B_y = \tilde{B}_y = 0$. Therefore, the numerical smoothing method introduced in this section serves as a fast and simple alternative to analytical approaches.

We compare the performance of the diffusive Galactic cosmic-ray propagation module in CRPropa 3.1 in the different field configurations in Section 4. Bilinear interpolation of the pre-computed \tilde{B}_r and \tilde{B}_z values on the (r, z) grid is used for the implementation of the convolved field. While this interpolation routine suffices for the present application

in a propagation algorithm with a high grid resolution, for MHD simulations one should rather choose a solenoidal interpolation routine based on, e.g., radial basis functions (McNally 2011) or the vector potential (Mackay et al. 2006).

4. PERFORMANCE COMPARISON IN CRPROPA

4.1. Test Setup

Besides the avoidance of an infinitely strong current sheet, the modifications to the JF12 field which were detailed above were also motivated by its application as the background field for Galactic cosmic-ray propagation simulations. The publicly available CRPropa 3.1 code (Alves Batista et al. 2016; Merten et al. 2017, see <https://crpropa.desy.de>) was used for testing the performance of the initial and modified JF12 fields in such applications. The low-energy extension of this code (module “DiffusionSDE”) is based on stochastic differential equations and propagates individual phase-space elements with an anisotropic diffusion tensor, such that the turbulent components of the GMF enter the simulation only implicitly. The algorithm uses an adaptive 5(4)-Fehlberg algorithm with Cash-Karp-coefficients (Cash & Karp 1990) in order to determine the tangent vector to the magnetic field at each step via field line integration. The tangent vector is then used to construct the local Frenet trihedron of the field line in which the actual propagation step is performed. Since the algorithm relies on field line integrations with adaptive step size, one may hope to reduce numerical errors and simulation time by introducing smoother field lines with larger radii of curvature.

In order to quantitatively compare the accuracy of the field line integration for different field configurations, the artificial test scenario of purely parallel diffusion with respect to the magnetic field lines was considered. The numerical error of the simulation may then be assessed by computing the spatial distance R of the phase space element position to its initial field line after a given trajectory length. As cosmic rays experience not only deflections in the parallel direction (along the magnetic field) but also perpendicular to it, such a simulation will most likely not reflect reality. However, pure parallel diffusion can be seen as the computationally most challenging limit for the field line integrator. Performing well in the case of pure parallel diffusion will most likely also result in good (or even better) performance in other, less idealized scenarios. For further discussions of realistic values of the ratio between parallel and perpendicular diffusion coefficients see, e.g., Shalchi (2009) and references therein.

In these tests, a total of $N = 10^7$ pseudo particles (“CRPropa candidates”) with a rigidity of $\rho = 1$ PV were propagated diffusively on trajectories with a maximum total length of 50 kpc. This particular rigidity was chosen as smaller rigidities lead to smaller step sizes and better results, whereas the diffusive transport approximation may not be valid at larger rigidities. The injection of these candidates was carried out randomly at 2000 source positions, which were uniformly distributed in a cylindrical volume with $1 \text{ kpc} \leq r < 15 \text{ kpc}$ and $|z| < 300 \text{ pc}$, avoiding the central region within 1 kpc. For these source positions, field lines were generated by second-order Heun integration with a fixed step size of 0.1 pc and a total length of 70 kpc. Concerning the step sizes r_{\min}, r_{\max} and relative error tolerance ε of the adaptive propagation module, the values $r_{\min} = 0.01 \text{ pc}$, $r_{\max} = 1 \text{ kpc}$, and $\varepsilon = 10^{-4}$ recommended by Merten et al.

(2017) were used. Finally, each candidate was deactivated upon either reaching the maximum trajectory length, entering a region without magnetic field, or leaving the simulation volume at a distance of 20 kpc from the origin. Afterwards, the minimum distance R between the particle’s final position and the initial field line was computed.

To ensure that field line integration via the Heun scheme is indeed able to generate nodes of the “reference field lines” that are sufficiently close to the analytical field lines which they are to represent, the minimum distance computation in the “X-field only” test cases (see below) was tentatively repeated by analytically computing the r_p and r_s labels of a particle’s initial and final positions in the initial JF12 and the parabolic X-field, respectively. The obtained differences of the mean field line deviations were found to be in the milliparsec range, thus justifying the use of the Heun method also for the full field, for which analytical field line labels are not available.

4.2. Results

Table 2 summarizes the parameters of performed tests and the respective performance results regarding both field line deviation and runtime, while Figure 5 displays the statistics of “field line fidelity” in each case. The ad hoc values for parameters z_s and δ were chosen for the simulations to test whether the introduction of these parameters is in principle able to improve the performance of the propagation algorithm. These numerical tests need to be repeated once a new fit of the modified JF12 model to observational data has been performed.

In the first set of tests, only the X-field was present. The left panel of Figure 5 clearly shows that, while the majority of pseudo particles stay relatively close to their respective field lines, the original JF12 X-field also generates a small number of cases with large excursions. It can also be seen that both smoothing methods are indeed able to eliminate most of these outliers. Together with the higher degree of “field line fidelity” – as indicated by generally much lower values of R –, this demonstrates that the smoothing achieves the desired effect as anticipated.

The second set of simulations uses the full large-scale field including, in particular, the toroidal halo and spiral disk field – modulated in z direction according to Equation (8) – with components replaced according to the bottom part of Table 2. Our new spiral field was not closed at the outer 20 kpc boundary of the simulation volume for these tests, but was allowed to extend unaltered up to the boundary of the computational domain. While the right panel of Figure 5 shows that the different smoothing methods did not completely eliminate all outliers, the mean and median deviations given in Table 2 indicate that the accuracy of the diffusion algorithm was improved in both cases, with the analytic smoothing methods giving the best results for the total field.

We finally note that, when interpreting these results and in particular the magnitude of typical R values, it should be kept in mind that pseudo-particle trajectories are not to be considered in isolation, and that the statistical weight of outliers, even those in the kiloparsec range, will be rather small in any ensemble of reasonable size. Note also that the exact results presented here depend on the chosen diffusion coefficient. A different choice of diffusion model or, e.g., rigidity of the pseudo-particles will certainly change the numbers but will most likely leave the general shape of the distributions unaltered.

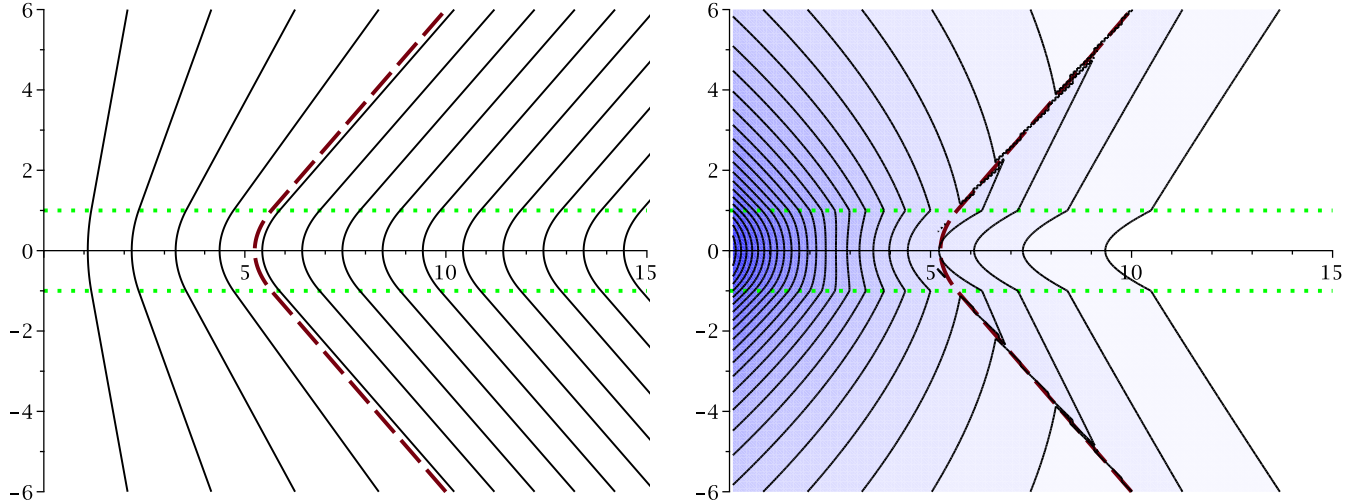


Figure 4. Field lines (left) and contours of $\|\mathbf{B}\|$ (right) in the poloidal (r, z) plane. The formerly wedge-shaped field (see Figure 5 in JF12) is smoothed within the $|z| \leq z_s = 1$ region (bounded by the green dotted lines). Note that the jump in field strength at the inner-outer separator field line (brown dashed line) is induced by the different scalings ($\propto r^{-1}$ vs. r^{-2}) of both regions according to Equations (19) and (21), and is therefore already present in the original JF12 field.

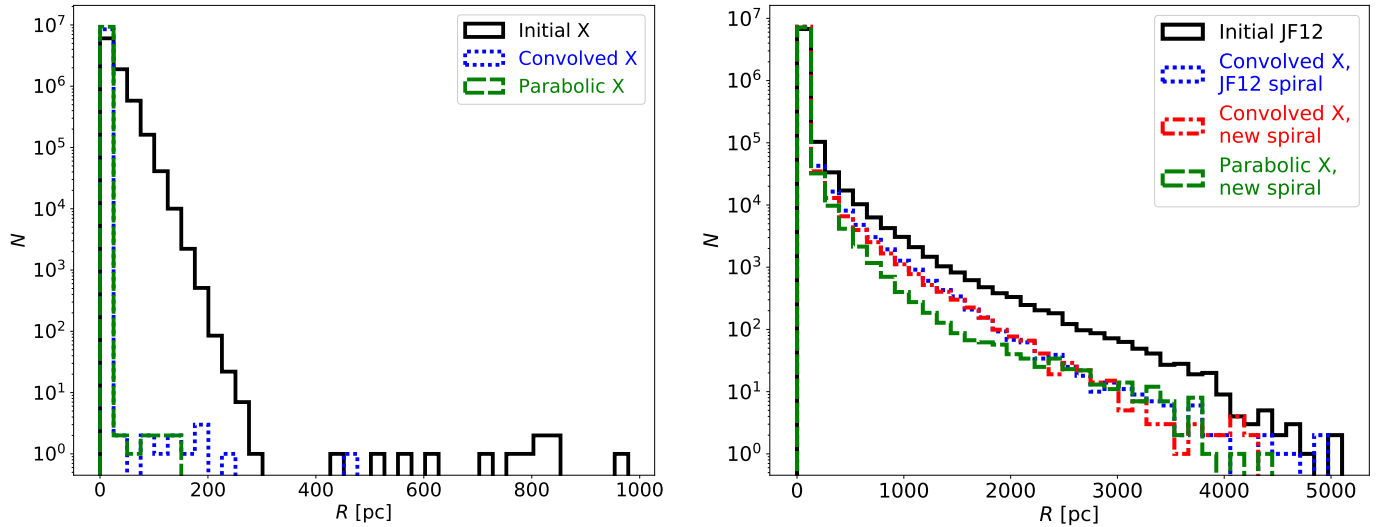


Figure 5. Histograms of field line deviations R of pseudo particles for purely parallel diffusion in different field configurations, comparing the initial JF12 field (black) with both the numerically convolved field (non-zero w_X , blue, as described in Section 3.5) and the X-field with parabolic insert (non-zero z_s , green, as described in Section 3.4). Left: X-field only. Particles on average stay much closer to their starting field line if a smoothed field is used, as indicated by generally smaller values of R . Note also the large excursions exhibited by a relatively small number of “outliers” which are present for the standard JF12 field but are mostly absent from both smoothed fields. Right: The same for the total large-scale field, consisting of spiral disk, molecular ring, X-field, and toroidal halo. The red data was generated in a simulation combining a numerically convolved X-field with a modified (“new”) spiral field that uses flux redistribution at r_1 and a value of r_2 exceeding the extent of the computational domain, thus corresponding to the black curve in Figure 2, while the standard JF12 spiral was used to obtain the blue data. Only particles whose deviation R exceeds 0.05 pc are taken into account. Simulation parameters may be found in Section 4.1 and Table 2.

Table 2

Results of the performance test simulations for different field configurations including the mean and median field line deviations of $N = 10^7$ pseudo particles with rigidity $\rho = 1$ PV, the mean call time of the `getField()` function in CRPropa, and the average time for a full test simulation. The presence of a factor of two between the smoothness parameters w_X and z_s applied for this comparison is justified in Appendix A.

Configuration	Parameters [kpc]	Mean deviation $\langle R \rangle$ [pc]	Median of R [pc]	Call time [μ s]	Simulation time [s]
Unmodified X-field only	–	18.17 ± 20.36	11.61	0.39	44.2 ± 1.1
Convolved X-field only	$w_X = 1.0$	0.22 ± 0.29	0.16	0.40	37.0 ± 1.2
Parabolic X-field only	$z_s = 0.5$	0.59 ± 0.57	0.43	0.41	33.4 ± 1.2
Unmodified JF12 field	–	16.20 ± 69.86	1.66	0.51	62.4 ± 0.8
Convolved X, JF12 spiral	$w_X = 1.0$	6.53 ± 43.19	0.45	0.54	62.9 ± 0.9
Convolved X, new spiral	$w_X = 1.0$; $\delta = 3.0$	6.01 ± 40.33	0.49	0.77	98.4 ± 1.0
Parabolic X, new spiral	$z_s = 0.5$; $\delta = 3.0$	5.08 ± 30.78	0.53	0.74	93.0 ± 0.9

Concerning the runtime for simulations in the different field configurations, the pure call time of the `getField()` function was evaluated 10^7 times. It is no surprise that the modified field calls take slightly longer as the evaluations are significantly more complicated than in the initial JF12 field. However, one might hope that less refinements of the adaptive field line integration step size are needed for smooth field lines, which could outweigh the call time disadvantage. Consequently, full test simulations with a more realistic 0.1 ratio of perpendicular to parallel diffusion (and all other settings as above) were conducted for the different field setups using $N = 10^6$ particles, and the average simulation time for five simulations was measured. As can also be seen from Table 2, the simulation times are indeed slightly reduced for the smoothed X-fields compared to the original JF12 X-field. On the other hand, the simulation runtime in the total field runs increased when a smoothed spiral field was used. In addition to the increased function call times, this is possibly also caused by the introduction of new field line kinks in the total field and the correspondingly increased number of subdivisions for the computation of the modified curved trajectories.

Finally, we note that these analytical improvements to the GMF model are going to be available with the latest version of the CRPropa software, at this time using parameters as given in Table 2. It can be used in the same way as the original implementation of the field in the `JF12Field` module.

5. SUMMARY AND CONCLUSIONS

In this work, we propose, derive, and discuss two major modifications to the popular JF12 model of the Galaxy’s large-scale magnetic field. The first of these modifications consists in the insertion of transition layers at the inner and outer rim of the spiral disk in which incoming and outgoing magnetic field lines are redistributed, resulting in the spiral field now being fully divergence-free also at its inner and outer boundary. As a possible alternative to the latter, the disk field could also be continued outwards indefinitely, thus avoiding an explicit flux closure by moving it to spatial infinity but incurring a possibly undesired excess in magnetic field energy.

The second, independent modification concerns the poloidal X-type field component and serves to remove the sharp kinks of field lines which the latter exhibits at the Galactic midplane. These kinks are either removed by a numerical convolution technique, or analytically replaced with smooth parabolic inserts, which also fully satisfy the divergence constraint. As a minor issue, we point out that the spherical cutout surrounding the origin can and should be removed to warrant solenoidality also near the Galactic center. A simple way to ensure the X-field’s solenoidality also at large distances is to depart from the original model by allowing the field to continue unaltered without explicit bounds. Although the very valid option of a dipolar field line closure at finite distances and with a finite energy content – now in the poloidal plane but otherwise in analogy to what we suggest at the inner spiral disk rim – exists as well, we refrain from a further investigation of this possibility at this point.

Finally, we employ both smoothing techniques for a quanti-

tative comparison in the framework of numerical cosmic-ray particle tracing using the CRPropa framework, and demonstrate the particles’ superior field line fidelity of the modified X-type field over its unmodified predecessor. A similar performance improvement could be found for the total field, with all suggested modifications performing on a comparable level. We speculate that the observed slight superiority of the analytical smoothing method might not necessarily prevail in other numerical settings.

In summary, we argue that, in addition to the observed performance improvement of the smoothed X-field in our exemplary CRPropa test runs, this modified field also represents a useful option for other applications, notably from the field of MHD simulations because it avoids an unphysically strong current sheet in the Galactic plane. On the other hand, many applications relying on a GMF may not at all be hampered by current sheets or kinking field lines. For those, the original, unsmoothed X-field clearly continues to be the model of choice due to its comparatively simpler form and ease of implementation. The divergence-free corrections of both the spiral and X-field, however, are crucial for physically relevant applications of the JF12 field model, and for this reason we consider it to be of high importance that they be taken into account in future studies. Therefore, all the modifications proposed in this work act to further improve on the usefulness and physical realism of the popular JF12 Galactic magnetic field model, which, however, will only come to full fruition once the extended set of parameters has been re-adjusted to ensure continued consistency with observational data.

ACKNOWLEDGMENTS

We are grateful to Horst Fichtner and the anonymous referee for valuable comments. Furthermore, JK acknowledges financial support through the *Ruhr Astroparticle and Plasma Physics (RAPP) Center*, funded as MERCUR project St-2014-040.

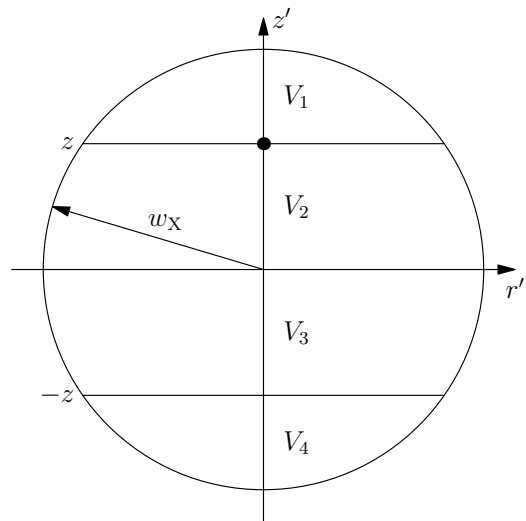


Figure 6. Partition of the spherical integration volume V into four vertically stacked sub-volumes $V_{1...4}$ to ease computation of the convolution integral (A3). B_r is negative for $z' > z$, i.e., in V_4 , and positive elsewhere.

APPENDIX

A. MATCHING SMOOTHING PARAMETERS

Since the analytical replacement method of Section 3.4 is very different from the convolution method of Section 3.5, a criterion is required that allows the respective smoothing constants z_s and w_X to be chosen such that the resulting fields are of comparable “smoothness.” To derive such a criterion, we employ the slightly simpler wedge-shaped field

$$B_z = 1, \quad B_r = \begin{cases} s & : z \geq 0 \\ -s & : z < 0 \end{cases} \quad (\text{A1})$$

with globally constant, rather than varying, inclination angle $\Theta_X^0 = \text{arccot}(s)$. We consider the two smoothed versions of this field to be equivalent for the purpose of the comparison detailed in Section 4 if their field lines have the same radius of curvature at $z = 0$. For the parabolic insertion method, this curvature radius follows directly from Equation (36) as

$$R_{\text{par}} = \left(\frac{\partial^2 r_F}{\partial z^2} \Big|_{z=0} \right)^{-1} = z_s \tan \Theta_X^0 = \frac{z_s}{s}. \quad (\text{A2})$$

Regarding the convolved field components \tilde{B}_r and \tilde{B}_z , we first note that $\tilde{B}_z = B_z = 1$, since B_z is a global constant. The convolution formula (44) for B_r reads

$$\tilde{B}_r(z) = \int_V B_r(z - z') K(\sqrt{r'^2 + z'^2}) 2\pi r' dr' dz' \quad (\text{A3})$$

and the integration volume V is a sphere of radius w_X centered on $(r', z') = (0, 0)$. Here we have implicitly set $r = 0$ without loss of generality because B_r is independent of r . Given that we will eventually set z equal to zero, we furthermore assume $z \in [0, w_X]$, also without loss of generality. As illustrated in Figure 6, V may be subdivided into four horizontally sliced cutouts $V_{1\dots 4}$ contained within the respective z' intervals $[-w_X, -z]$, $[-z, 0]$, $[0, z]$, and $[z, w_X]$. Because $B_r = +s$ in $V_{1\dots 3}$ and $B_r = -s$ in V_4 , we see that the contributions from V_2 and V_3 are equal, while those from V_1 and V_4 cancel. It is therefore sufficient to perform the integration of Equation (A3) just over V_3 – in which $B_r = s$ is a constant – and then double the result. We may thus compute the radius of curvature of the convolved field at $z = 0$ according to

$$\begin{aligned} \frac{1}{R_{\text{con}}} &= \frac{\partial}{\partial z} \left(\frac{\tilde{B}_r}{\tilde{B}_z} \right) \Big|_{z=0} = \frac{\partial}{\partial z} \left(2s \int_0^z \int_0^{\sqrt{w_X^2 - z'^2}} K(\sqrt{z'^2 + r'^2}) 2\pi r' dr' dz' \right) \Big|_{z=0} \\ &= 4\pi s \int_0^{\sqrt{w_X^2 - z^2}} K(\sqrt{z^2 + r'^2}) r' dr' \Big|_{z=0} = 4\pi s \int_0^{w_X} K(r') r' dr' \\ &= 4\pi s \mathcal{N} \int_0^1 \exp[(u^2 - 1)^{-1}] w_X^2 u du = 4\pi s \mathcal{N} w_X^2 J_1 \end{aligned} \quad (\text{A4})$$

with the shorthand definition

$$J_n \equiv \int_0^1 u^n \exp[(u^2 - 1)^{-1}] du. \quad (\text{A5})$$

Inserting the normalization condition

$$\frac{1}{\mathcal{N}} = \int_0^{w_X} K(r') 4\pi r'^2 dr' = 4\pi \int_0^1 \exp[(u^2 - 1)^{-1}] w_X^3 u^2 du = 4\pi w_X^3 J_2 \quad (\text{A6})$$

of kernel K into Equation (A4) leads us to $R_{\text{con}} = (J_2/J_1)(w_X/s)$. The condition $R_{\text{par}} = R_{\text{con}}$ is therefore equivalent to

$$\frac{w_X}{z_s} = \frac{J_1}{J_2} \approx 2.114, \quad (\text{A7})$$

independently of inclination angle. This justifies choosing parameters of ratio $w_X/z_s = (1 \text{ kpc})/(500 \text{ pc}) = 2$ in Table 2.

REFERENCES

- Alves Batista, R., Dundovic, A., Erdmann, M., et al. 2016, JCAP, 5, 038
 Beck, M. C., Beck, A. M., Beck, R., et al. 2016, JCAP, 5, 056
 Beck, R. 2009, Ap&SS, 320, 77
 Boulanger, F., Enßlin, T., Fletcher, A., et al. 2018, JCAP, 8, 049
 Brackbill, J. U., & Barnes, D. C. 1980, J. Comput. Phys., 35, 426
 Brown, J. C., Haverkorn, M., Gaensler, B. M., et al. 2007, ApJ, 663, 258
 Cash, J. R., & Karp, A. H. 1990, ACM Trans. Math. Softw., 16, 201
 Ferrière, K., & Terral, P. 2014, A&A, 561, A100
 Jansson, R., & Farrar, G. R. 2012, ApJ, 757, 14
 Mackay, F., Marchand, R., & Kabin, K. 2006, JGR (Space Phys.), 111, A06205
 McNally, C. P. 2011, MNRAS, 413, L76
 Merten, L., Becker Tjus, J., Fichtner, H., Eichmann, B., & Sigl, G. 2017, JCAP, 1706, 046
 Oliphant, T. E. 2007, Computing in Science & Engineering, 9, 10

Shalchi, A. 2009, *Astrophysics and Space Science Library*, Vol. 362, *Nonlinear Cosmic Ray Diffusion Theories* (Springer), doi:10.1007/978-3-642-00309-7

Shukurov, A., Rodrigues, L. F. S., Bushby, P. J., Hollins, J., & Rachen, J. P. 2019, *A&A*, 623, A113
Terral, P., & Ferrière, K. 2017, *A&A*, 600, A29
Unger, M., & Farrar, G. 2019, arXiv e-prints, arXiv:1901.04720
Unger, M., & Farrar, G. R. 2017, *Int. Cosmic Ray Conf.*, 35, 558